ADVANCED QUANTUM TECHNOLOGIES
www.advquantumtech.com

Benchmark for Synthesized Diamond Sensors Based on Isotopically Engineered Nitrogen-Vacancy Spin Ensembles for Magnetometry Applications

Christian Osterkamp, Priyadharshini Balasubramanian,* Gerhard Wolff, Tokuyuki Teraji, Milos Nesladek, and Fedor Jelezko*

Nitrogen-vacancy (NV) center ensemble in synthetic diamond is a promising and emerging platform for quantum sensing technologies. Realization of such a solid-state based quantum sensor is widely studied and requires reproducible manufacturing of NV centers with controlled spin properties, including the spin bath environment within the diamond crystal. Here, a non-invasive method is reported to benchmark NV ensembles regarding their suitability as ultra-sensitive magnetic field sensors. Imaging and electron spin resonance techniques are presented to determine operating figures and precisely define the optimal material for NV-driven diamond engineering. The functionality of the methods is manifested on examples of chemical vapor deposition synthesized diamond layers containing preferentially aligned, isotopically controlled ^{15}NV center ensembles. Quantification of the limiting ^{15}N P1 spin bath, in an otherwise ^{12}C enriched environment, and the reduction of its influence by applying dynamical decoupling protocols, complete the suggested set of criteria for the analysis of NV ensemble with potential use as magnetometers.

An essential task toward the implementation of scalable quantum technology is to bridge the gap between quantum physics on the sub nanoscale and material science engineering capabilities on the macroscale. Quantum-enhanced sensing based on nitrogen-vacancy (NV) centers is a novel ultra-sensitive methodology for nanoscale detection of magnetic[1] and electric fields,[2] temperature,[3] pressure, and force.[4,5] However, these sensing methods need to be matched with diamond engineering in order to create the NV atomic defect sensors reliably in synthetic diamond. NV center based sensors have been extensively studied in the past, where long coherence times, optical accessibility of spin states, and ambient working conditions were demonstrated.[6] Furthermore, nanoscale magnetic resonance imaging with NV centers shows potential applications toward investigating more complex biological systems like neural networks,[7] living cells,[8] and single proteins.[9] Transferring these sensors to state-of-the-art quantum technology requires the reproducible fabrication of NV centers with high spatial precision and reliable spin coherence properties.[10,11]

Nitrogen doping during chemical vapor deposition (CVD) diamond growth is one of the facile means of fabricating thin layers of shallow NV ensembles.[12] It is essential for ultra-sensitive nanoscale magnetometry that shallow NV centers are engineered to be placed in a close proximity to the sensing target. Furthermore, the CVD growth method offers a crucial advantage in producing different orientations of diamond layers and for the {111} orientation, NV ensembles are preferentially aligned with the ⟨111⟩ direction. Studies show up to 99% orientational polarization of NVs in samples grown along

C. Osterkamp, P. Balasubramanian, G. Wolff
Institute for Quantum Optics and Center for Integrated Quantum Science and Technology (IQST)
Ulm University
Albert Einstein Allee 11, Ulm 89081, Germany
E-mail: christian.osterkamp@uni-ulm.de; priyadharshini.balasubramanian@uni-ulm.de

Dr. T. Teraji
Wide Bandgap Materials Group
Research Center for Functional Materials
National Institute for Material Science
1-1, Namiki Tsukuba, Ibaraki 305-0044, Japan

Prof. M. Nesladek
Institute for Materials Research (IMO)
Hasselt University
Wetenschapspark 1, B-3590 Diepenbeek, Belgium

Prof. F. Jelezko
Institute for Quantum Optics and Center for Integrated Quantum Science and Technology (IQST)
Ulm University
Albert Einstein Allee 11, Ulm 89081, Germany

The ORCID identification number(s) for the author(s) of this article can be found under https://doi.org/10.1002/qute.202000074

DOI: 10.1002/qute.202000074

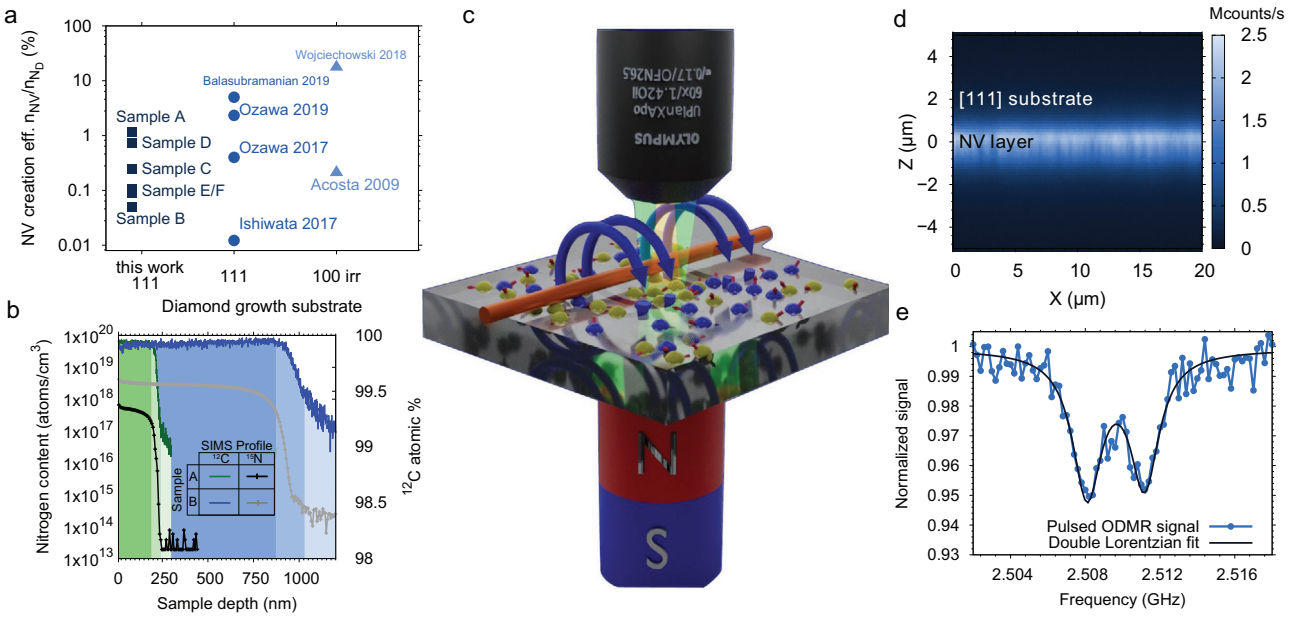

Figure 1. a) Overview of created NV centers in comparison to the nitrogen present in the diamond layer n_{NV}/n_{N_D} for different CVD growth processes from this work, related work,[13–15,18] and work covering electron irradiated and annealed ⟨100⟩ samples.[30,31] b) SIMS measurement showing the depth profile of the carbon (^{12}C) and nitrogen (^{15}N) content in samples A and B. The pale-colored area indicates the diamond substrate, the intermediate color the buffer layer, and the dark color the nitrogen-doped layer. c) Schematic drawing of the wide-field set-up used to perform sample analysis. d) Confocal image showing the cross-section of the CVD grown layer on top of the ⟨111⟩ substrate. e) ODMR spectrum showing the characteristic splitting of 3.03 MHz due to the hyperfine interaction with the intrinsic ^{15}N.

the ⟨111⟩ crystal direction.[13–15] For quantum sensing applications, such engineered diamond samples inherently improve the sensor sensitivity by a factor of four while retaining the high SNR. Furthermore, usage of oriented NV samples are particularly beneficial for zero-field applications which extend the dynamic range of the magnetometer.[16,17] Compared to the low-energy ion implantation technique, nitrogen incorporation (e.g., N doping) during diamond growth avoids the collateral damage of the crystal lattice, thus improving the spin environment of individual NV centers. Although some demonstration of enhanced magnetometry with preferentially aligned ensembles has been achieved,[18,19] the coherence time and the ensembles' density remain as critical limitations toward realistic applications.

One of the primary reasons is the low N to NV creation efficiency in these samples. **Figure 1**a compares the NV to N_D (nitrogen content in diamond solid phase) ratio for different methods reported so far. Although the nitrogen incorporation rate is higher along the ⟨111⟩ growth direction, the NV creation efficiency is small for all types of as-grown diamonds. The number of NVs in the sample can be significantly improved through electron irradiation and high-temperature annealing treatments. However, this comes at the cost of lattice damages implying low coherence times and the loss of preferential orientation.[19,20] Another subtle approach is to tune the growth parameters in order to improve the NV incorporation during crystal growth. In this regard, a recent study shows the temperature dependence of NV incorporation in a ⟨113⟩-oriented diamond substrate while retaining preferential orientation.[21] The sub-optimal creation efficiency also implies a strong magnetic noise from the remaining nitrogen impurities, which reduces the coherence time and, therefore, the maximal sensing time of the NV ensembles. A recent review discusses these limitations in the context of quantum sensing applications,[22] showing the imminent need to optimize the creation process of NV centers.

In this work, we report on the role of nitrogen on the diamond growth process, the NV creation efficiency, and the coherence time limiting spin bath in ⟨111⟩ growth direction. To this end, we prepare and study the performance of six potential diamond magnetometers. Application of our benchmark criteria leads to an enhanced production process since key figures can be isolated and their optimization can be performed separated from other system parameters. The core criteria consist of the overall NV center density, the NV/P1 center ratio, and the dynamical decoupling scaling constant κ. The latter two are of major importance since they limit the coherence time of the NV ensembles and contain information about the surrounding spin bath. The identification of these values is of significant importance since the comparability and reproducibility of suitable NV layers are crucial for the fabrication of reliable magnetometers with industrial applications.

The samples studied in this work are prepared in-house using the home-built plasma-enhanced chemical vapor deposition (PECVD) system. The diamond substrates are ⟨111⟩ oriented IIa type diamond crystals produced by New Diamond Technology company (samples A–C, F) and Applied Diamond Inc (samples D+E). In order to investigate the role of gas-phase nitrogen on the nitrogen incorporation efficiency during PECVD diamond growth, we synthesize three diamond samples with varying ^{15}N nitrogen content with respect to hydrogen (N/H) in the growth chamber (samples A:0.1%, B:1%, and C:5%). Growth

temperature, measured via an infra-red pyrometer, was set to 1005°C for samples A–C. The effect of a varying growth temperature is studied using another three samples, under a constant nitrogen content of 0.1% (samples D: 1005°C; E: 965 °C; and F: 1035°C). A detailed description of all samples can be found in Supporting Information. Prior to the inclusion of nitrogen gas, an intrinsic buffer layer was deposited on top of each substrate to ensure the isotopic purity (>99.99% ^{12}C) of the nitrogen hosting diamond layer. Following the buffer layer, ^{15}N nitrogen gas is introduced into the growth chamber. The growth duration of the N doped layer was adjusted to be three times longer than the growth time for the intrinsic one. Evaluation of the materials' isotopic purity and the nitrogen composition is achieved using secondary ion mass spectrometry (SIMS), confocal and wide-field imaging and electron spin resonance (ESR) techniques. The nitrogen content in the overgrown diamond samples A and B are measured using SIMS and the results are shown in Figure 1b.

The results evidence that an elevated gas phase nitrogen concentration leads to a higher nitrogen presence in the solid phase. Nitrogen concentration in the gas phase (N/H) for the three samples A, B, and C in the relative content of 1:10:50, implicates a nitrogen ratio of 1:5.42:10.54 within the diamond, where the absolute values are 41 ppm for sample A, 222 ppm for sample B, and 432 ppm for sample C. Note that these values indicate the upper limit of all forms of nitrogen impurities (N, NV, NVH) in the overgrown diamond layer and acts as a reliability test for the presented benchmark techniques. The second exciting feature is the different growth rates due to the varied nitrogen gas-phase concentrations, where a higher nitrogen percentage causes a higher growth rate. A tenfold increased nitrogen content yields a 1.2 times increased growth rate for sample B (7.29 nm min^{-1}) with respect to sample A (6.33 nm min^{-1}). The growth rate for the produced buffer layer scales linearly in time and reaches a value of 5.00 and 5.17 nm min^{-1} for samples A and B, respectively.

Higher growth temperatures speed-up and lower temperatures slow-down the diamond growth as shown in Supporting Information, where samples E and F reach growth rates of 6.60 and 7.80 nm min^{-1}, respectively. NV center concentrations within the nitrogen-rich diamond layers are determined by evaluating images recorded with a confocal and wide-field setup, where the latter is depicted in Figure 1c. An area of approximately 10 μm^2 is illuminated with a widened, collimated laser beam, in order to excite the NV ensemble. The emitted fluorescence is then captured, and the signal is normalized with the count rate of a single NV. A cross-sectional confocal image used for this normalization procedure is shown in Figure 1d. Using this method, NV density in sample A is estimated to be around 464 ppb. Note that a reliable NV center density estimation requires identical experimental conditions under which the fluorescence rate from the ensemble and the single NV (preferably in a ⟨111⟩-diamond) is measured.

In order to confirm that the fluorescence originate from the NVs embedded in the grown layer, we apply the pulsed optically detected magnetic resonance (ODMR) technique. In Figure 1e, we plot the pulsed ODMR measurement showing the characteristic hyperfine splitting (3.03 MHz) due to the ^{15}N nuclear spin.[6] Since the natural abundance of ^{15}N is only 0.36 %, we conclude that the detected fluorescence originates from the NVs produced due to intentional nitrogen doping. Note that all investigated NV center ensembles of all samples A–F are preferentially-aligned along the ⟨111⟩ crystal axis, independent of the executed growth process or use of diamond substrate. During the N doping PECVD diamond growth step, a nitrogen atom can be substituted in the growing surface layer, followed by the incorporation of a lattice vacancy. Since this is the energetically favorable configuration, a preferential creation along one axis is the result of this PECVD overgrowth of ⟨111⟩ oriented diamond substrates.[23,24] The preferential alignment is proven by ODMR measurements as reported in Ref. [18].

We now focus on one of the predominant forms of nitrogen impurities in such nitrogen-doped CVD samples. Early EPR studies show that substitutional nitrogen impurities called P1 centers usually outnumber other types of nitrogen defects in the diamond lattice.[25] The P1 centers are essential for the formation and charge stabilization of the NV centers. Additionally, in a ^{12}C enriched diamond crystal, the paramagnetic P1 centers present the dominant noise source for NV ensembles. Hence, the NV/P1 ratio is a good figure of merit for potential diamond sensors and gives room for improvement for NV driven diamond engineering using CVD methods. Thus, central to this work is the careful quantification of P1 and NV spin densities in the prepared sample. As the samples host a thin layer of paramagnetic impurities, it is difficult to estimate the spin densities using standard bulk EPR techniques. Therefore, we use the NV ensembles to probe its magnetic field environment. Here, we utilize spin-echo based double electron-electron resonance (DEER) technique to quantify the density of the P1 spin bath.

We first identify the bath spectrum using the spin-echo double electron resonance protocol. The sequence is composed of a spin-echo on the NVs with a synchronous inversion of the bath spins. The π pulse on the bath spins reintroduces the static dipolar interaction with the NVs, thus causing an observable decrease in the echo amplitude. **Figure 2**a shows the measured P1 spectrum at an external magnetic field $B_0 \approx 330$ G, aligned parallel to the ⟨111⟩ axis. The observed spectrum matches the characteristic ^{15}N nitrogen P1 transition frequencies, where the two outer lines (groups I and IV) correspond to the hyperfine transitions of P1 spins parallel to B_0. The prominent inner lines (groups II and III) correspond to the hyperfine transition of the other three magnetically equivalent P1 orientations. The weak central peak is due to the dipole forbidden transitions of the ^{15}N nitrogen electron spins. We emphasize that the observed spectrum does not show any spectral features corresponding to $g = 2$ or NVH spin transitions. Further analysis of the P1 bath spectrum is discussed in Supporting Information.

In order to determine the P1 spin bath density, we use the pulse sequence depicted in Figure 2b. The bath π pulse addressing one of the P1 transitions is swept during the second free precession time of the NV echo sequence. This time-swept sequence controls the degree to which the P1 dipolar interactions are reintroduced. These static dipolar interactions lead to a mono-exponential decay of NV coherence, which depends on the density of the inverted bath spins and their decoupling time T. The DEER experiment is repeated for each P1 transition and the results for sample D are shown in Figure 2b. The measured data is fit with a mono-exponential function of the form $\exp[-A\gamma_{NV}\gamma_{bath}n_{bath}T]$, where $A\gamma_{NV}\gamma_{bath} \approx 292$ kHz ppm^{-1}.[26] The results show that the density of P1 groups I–IV are $4.9 \pm 0.15, 10.9 \pm 0.25, 11.6 \pm 0.19, 5.0 \pm 0.15$ ppm, respectively.

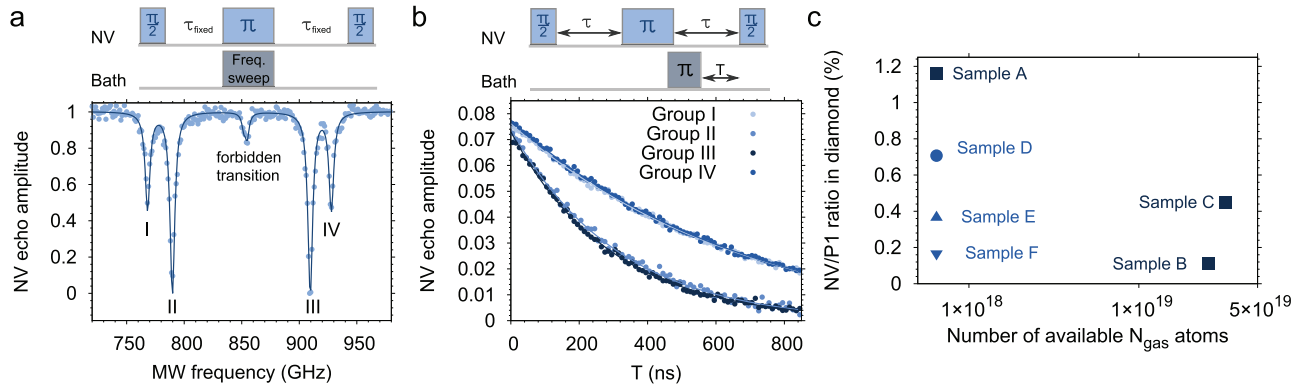

Figure 2. a) Measured ^{15}N nitrogen P1 bath spectrum with the corresponding pulse sequence. The spectrum is obtained at $B_0 \approx 330$ G aligned parallel to ⟨111⟩ direction. The solid line corresponds to the simulated P1 spectrum with a common linewidth and amplitude matching their spectral abundance. b) Estimation of P1 bath density. The solid line corresponds to the mono-exponential fit function of the form $\exp[-A\gamma_{NV}\gamma_{bath}n_{bath}T]$, where $A\gamma_{NV}\gamma_{bath} \approx 292$ kHz ppm^{-1}. c) Estimated NV/P1 ratio received for the samples A–F of this study in relation to the maximum available number of ^{15}N atoms in the growth chamber.

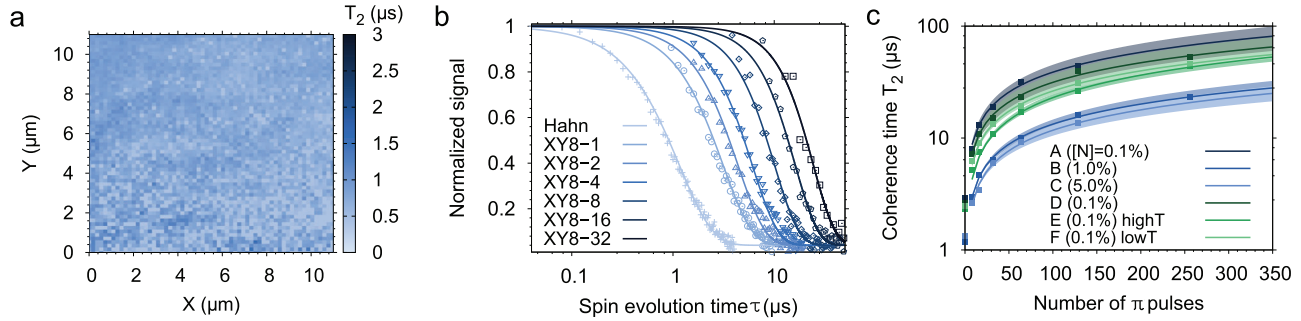

Figure 3. a) Hahn Echo measurements performed on sample B with the wide-field setup. The illustrated area is subdivided into 64 x 64 pixels, where each pixel represents the fitted decay time of a Hahn echo measurement. The image indicates a rather uniform distribution among coherence times of the created ensembles. b) A Hahn Echo measurement performed on an ensemble of sample B with the confocal microscope setup. Additional dynamical decoupling protocols are applied to prolong the coherence time from initial $T_2^{Hahn} = 1.2\,\mu s$ up to $T_2^{XY8-32} = 23\,\mu s$. c) Saturation behavior of the XY8 dynamical decoupling protocols applied to samples A–F. Solid lines represent fit functions (fit errors are illustrated as colored area) based on a power scaling law ($T_2 \propto N^{\kappa}$) with a free parameter κ. Remarkable is that all samples show similar values ($\kappa_A = 0.59$, $\kappa_B = 0.59$, $\kappa_C = 0.60$, $\kappa_D = 0.58$, $\kappa_E = 0.66$, and $\kappa_F = 0.59$) suggesting a Lorentzian distributed spin bath, where the decoherence originates from one spin type.[28,29]

Hence the total measured ^{15}N substitutional nitrogen density is ≈ 32 ppm. Since the main interest of the study is the optimization of NV density during CVD growth, we compare the NV/P1 ratios in the prepared samples A–F. Estimation of NV center density is a difficult task, and proper estimation methods are still under investigations.[19,26] The technique used to perform the NV density estimation is, similar to the one presented in ref. [19]. In Figure 2c, we show the NV/P1 ratio as a function of gas-phase nitrogen concentration inside the PECVD growth chamber. Clearly visible is that sample A shows the best NV/P1 ratio of approximately 1.2%, which is of the same order of magnitude as previously reported values for nitrogen-doped CVD layers.[25] The low N/C ratio of the source gases, in combination with the intermediate growth temperature of 1005 °C promotes the formation of NV centers while keeping a high conversion rate from P1 to NV. A possible explanation is that the NV formation kinetics is slower than the nitrogen incorporation (P1 formation), which is supported by the reported NV/P1 ratios in bulk diamond samples.[25] A low N concentration though, decelerates the diamond growth and gives NV defects sufficient time for the formation. A further hint supporting this hypothesis is that the variation of growth temperature shifts the NV/P1 ratio in disadvantage of NV creation (samples E and F). An increased and decreased temperature leads to an elevated growth rate (see Supporting Information) but a decreased NV/P1 ratio. Obviously, this has to be studied in more detail in the future, but the temperature dependence on NV creation is in agreement with results of other groups.[21]

Another relevant parameter for the realistic application of NV magnetometry is the uniformity of sensor spin coherence across the sample volume. **Figure 3**a shows this circumstance, where the Hahn echo coherence time is measured over a large area using the wide-field setup.

The coherence times measured among sample B are on the order of 1 μs, which is limited by the electronic spin bath. Decoherence from an electronic spin bath can be effectively mitigated through quantum control of the spin bath or through dynamical decoupling sequences. The latter is known to artificially prolong the coherence time since only the influence and not the spin bath itself is reduced, which is desired from a material scientist's point of view. The XY8 sequence is chosen

Table 1. Summary of the results received for the six diamond samples investigated in this work.

Sample	Temp	N/H	d_{buffer}	d_{NV}	T_2^*	T_2	$T_2^{XY8\text{-}16}$	n_{NV}	n_{P1}	n_{N_D}	η_V^{ac}
	[°C]	[%]	[nm]	[nm]	[ns]	[µs]	[µs]	[ppb]	[ppm]	[ppm]	$[\frac{nT\sqrt{\mu m^3}}{\sqrt{Hz}}]$
A	1005	0.1	50	190	180	3.2	44	464	40	41	0.26
B	1005	1.0	155	875	40	1.0	15	109	100	222	0.95
C	1005	5.0	25	66	42	1.3	13.5	447	100	432	0.41
D	1005	0.1	50[a)]	190[a)]	31	2.6	38.7	290	32	41	0.36
E	965	0.1	66	235	200	2.4	26.1	181	50(3)	73	0.47
F	1035	0.1	78	320	57	2.5	31.1	69	42	77	0.75

The growth temperature is labeled as Temp, the nitrogen gas concentration during the growth in respect to hydrogen as N/H, the thickness of the buffer layer as d_{buffer}, the one of the NV rich layer as d_{NV}, the dephasing time measured by Ramsey sequence as T_2^*, the coherence time measured by Hahn echo as T_2, the artificially prolonged coherence time by XY8 sequence with 128 π-pulses as $T_2^{XY8\text{-}16}$, the NV density as n_{NV}, the P1 density as n_{P1}, the overall nitrogen density measured by SIMS n_{N_D}, and the estimated volume normalized ac magnetic field sensitivity as η_V. The latter's estimation was performed using a pulsed detection scheme with a readout laser pulse of $\tau_l = 300$ ns, full spin contrast, and a count rate of a single NV center $c_R = 200$ kcts s^{-1} as reported in ref. [1,18,32]. Conditions of the growth processes are microwave (MW) frequency $f = 2.46$ GHz, MW power $P = 1.92$ kW, pressure $p = 52.5$ mbar, methane concentration $c_M = 0.1$ % with respect to hydrogen which was applied with a flow of 400 sccm. [a)] Estimated from SIMS results of sample A, which was grown under identical conditions.

to perform this task[27] and therefore increase the sensitivity of a quantum sensor. The results of an ensemble from sample B, which is dynamically decoupled with different orders of the XY8-N sequence, where N denotes the number of repetitions of 8 π-pulses, is shown in Figure 3b. The saturation behavior of this decoupling allows a conclusion on the underlying decoherence causing spin bath. For this purpose, all samples are investigated with the XY8 technique and the measured coherence times scale equally for samples A–F (see Figure 3c). The data points of each sample are fitted with a power-law of the form ($T_2 \propto N^{\kappa}$), where the κ_{A-F} values are very similar to $\kappa = 2/3$, a value which has been reported earlier and is associated with a Lorentzian distributed noise source.[28,29] Since we are working in a nearly ^{13}C free spin environment, our interpretation of this factor is that the NV ensembles are mainly limited by one spin species, which we identify as P1 centers. Furthermore, this also shows the effectiveness of dynamical decoupling for extending the coherence time of the spin ensembles. For all samples at least an order of magnitude improvement was measured.

Table 1 contains all samples used during this work and the corresponding results of various measurements presented here. Note that the column η_V^{ac} (normalized ac magnetic field sensitivity) was calculated using the following equation:

$$\eta_V^{ac} = \frac{\hbar}{g \times \mu_B} \times \frac{1}{C_0 \times \sqrt{n \times c_R \times \tau_l \times T_2}} \quad (1)$$

where $\hbar$, g, μ_B are the reduced Planck constant, the Landé g-factor, and the Bohr magneton, respectively. C_0 denotes the measurement contrast, $n = N/V$ the NV density (N: number of NV centers, V: examined diamond volume), c_R the emission rate of a single NV center, τ_l the laser pulse duration, and T_2 the coherence time as measured by the Hahn echo sequence.

Using the proposed standard of comparison, it is possible to find the best growth strategy for the fabrication of NV center ensembles, with respect to the primary decoherence source, which we identify as P1 centers. Clearly, the growth procedure for sample A is the most promising one, with superior magnetic field sensitivity, since not only the measured interaction times are among the longest but also the absolute NV concentration is the highest, at a moderate background level of P1 centers. Note that in this work a subset of all possible NV fabrication parameters are discussed, namely nitrogen gas concentration and growth temperature. Many more have to be optimized in order to push the sensitivity to its limit. Hints for this are the different NV/P1 ratios of samples A and D, which were created under the same plasma conditions. This can probably be related be related to differences in the diamond substrates provided by different suppliers. Besides the crystallinity and the surface roughness, the surface miscut-angle is probably the most influencing parameter. The influence of these substrate related parameters on the NV creation, though, was not studied during this work.

In conclusion, we have presented a new benchmark for NV center ensembles in a thin layer of diamond produced during a PECVD growth process. The characterization techniques exploit the core feature of the NV center itself, namely its sensing capability. This feature can be used to isolate main driving parameters influencing the NV/P1 ratio and to improve PECVD diamond growth processes with the distinct goal to fabricate NV center ensembles for magnetometry applications. Furthermore, by applying the presented benchmark criteria, NV rich diamond samples can be analyzed and, more importantly, ranked for an unbiased comparison among several production techniques enabling potential synergistic effects that accelerate the development of optimized diamond samples, which are indispensable toward real-life quantum technology applications.

Supporting Information

Supporting Information is available from the Wiley Online Library or from the author.

Acknowledgements

C.O., P.B., and G.W. contributed equally to this work. The authors thank Christoph Findler for experimental support and PD Boris Naydenov for fruitful discussions. The authors would like to thank Cambridge Isotope Laboratories Inc. for the support of this project. This work was supported by DFG (Quantum + Grade, POLis), BMBF (Diaquantfab, Microsens, QMagine, Nanospin), EU (ERC Synergy Grants BioQ and HyperQ, Quantera project), Volkswagenstiftung, and IQST. M.N. acknowledges support of Belgian FWO – SB) project DIAQUANT, and T.T. achnowledges the support of JSPS KAKENHI (no. 20H02187, 19H02617, and 16H06326), JST CREST (no. JPMJCR1773), and MEXT Q-LEAP (no. JPMXS0118068379), Japan.

Open access funding enabled and organized by Projekt DEAL.

Conflict of Interest

The authors declare no conflict of interest.

Keywords

CVD diamond growth, nitrogen-vacancy centers, preferential alignment, quantum sensing

Received: July 17, 2020
Revised: August 12, 2020
Published online: August 28, 2020

[1] L. Rondin, J.-P. Tetienne, T. Hingant, J.-F. Roch, P. Maletinsky, V. Jacques, *Rep. Prog. Phys.* **2014**, *77*, 056503.
[2] F. Dolde, H. Fedder, M. W. Doherty, T. Nöbauer, F. Rempp, G. Balasubramanian, T. Wolf, F. Reinhard, L. C. L. Hollenberg, F. Jelezko, J. Wrachtrup, *Nat. Phys.* **2011**, *7*, 459.
[3] G. Kucsko, P. C. Maurer, N. Y. Yao, M. Kubo, H. J. Noh, P. K. Lo, H. Park, M. D. Lukin, *Nature* **2013**, *500*, 54.
[4] J. Cai, F. Jelezko, M. B. Plenio, *Nat. Commun.* **2014**, *5*, 4065.
[5] M. S. J. Barson, P. Peddibhotla, P. Ovartchaiyapong, K. Ganesan, R. L. Taylor, M. Gebert, Z. Mielens, B. Koslowski, D. A. Simpson, L. P. McGuinness, J. McCallum, S. Prawer, S. Onoda, T. Ohshima, A. C. Bleszynski Jayich, F. Jelezko, N. B. Manson, M. W. Doherty, *Nano Lett.* **2017**, *17*, 1496.
[6] M. W. Doherty, N. B. Manson, P. Delaney, F. Jelezko, J. Wrachtrup, L. C. Hollenberg, *Phys. Rep.* **2013**, *528*, 1.
[7] L. T. Hall, G. C. G. Beart, E. A. Thomas, D. A. Simpson, L. P. McGuinness, J. H. Cole, J. H. Manton, R. E. Scholten, F. Jelezko, J. Wrachtrup, S. Petrou, L. C. L. Hollenberg, *Sci. Rep.* **2012**, *2*, 401.
[8] D. Le Sage, K. Arai, D. R. Glenn, S. J. DeVience, L. M. Pham, L. Rahn-Lee, M. D. Lukin, A. Yacoby, A. Komeili, R. L. Walsworth, *Nature* **2013**, *496*, 486.
[9] I. Lovchinsky, A. O. Sushkov, E. Urbach, N. P. de Leon, S. Choi, K. de Greve, R. Evans, R. Gertner, E. Bersin, C. Müller, L. McGuinness, F. Jelezko, R. L. Walsworth, H. Park, M. D. Lukin, *Science* **2016**, *351*, 836.
[10] J. L. Webb, J. D. Clement, L. Troise, S. Ahmadi, G. J. Johansen, A. Huck, U. L. Andersen, *Appl. Phys. Lett.* **2019**, *114*, 231103.
[11] F. M. Stürner, A. Brenneis, J. Kassel, U. Wostradowski, R. Rölver, T. Fuchs, K. Nakamura, H. Sumiya, S. Onoda, J. Isoya, F. Jelezko, *Diamond Relat. Mater.* **2019**, *93*, 59.
[12] A. Stacey, D. A. Simpson, T. J. Karle, B. C. Gibson, V. M. Acosta, Z. Huang, K. M. C. Fu, C. Santori, R. G. Beausoleil, L. P. McGuinness, K. Ganesan, S. Tomljenovic-Hanic, A. D. Greentree, S. Prawer, *Adv. Mater.* **2012**, *24*, 3333.
[13] H. Ozawa, K. Tahara, H. Ishiwata, M. Hatano, T. Iwasaki, *Appl. Phys. Express* **2017**, *10*, 045501.
[14] H. Ozawa, Y. Hatano, T. Iwasaki, Y. Harada, M. Hatano, *Jpn. J. Appl. Phys.* **2019**, *58*, SI SIIB26.
[15] H. Ishiwata, M. Nakajima, K. Tahara, H. Ozawa, T. Iwasaki, M. Hatano, *Appl. Phys. Lett.* **2017**, *111*, 043103.
[16] P. London, P. Balasubramanian, B. Naydenov, L. P. McGuinness, F. Jelezko, *Phys. Rev. A* **2014**, *90*, 1.
[17] H. Zheng, J. Xu, G. Z. Iwata, T. Lenz, J. Michl, B. Yavkin, K. Nakamura, H. Sumiya, T. Ohshima, J. Isoya, J. Wrachtrup, A. Wickenbrock, D. Budker, *Phys. Rev. Appl.* **2019**, *11*, 6.
[18] P. Balasubramanian, C. Osterkamp, Y. Chen, X. Chen, T. Teraji, E. Wu, B. Naydenov, F. Jelezko, *Nano Lett.* **2019**, *19*, 6681.
[19] C. Osterkamp, M. Mangold, J. Lang, P. Balasubramanian, T. Teraji, B. Naydenov, F. Jelezko, *Sci. Rep.* **2019**, *9*, 5786.
[20] J. Achard, V. Jacques, A. Tallaire, *J. Phys. D: Appl. Phys.* **2020**, *53*, 313001.
[21] S. Chouaieb, L. J. Martínez, W. Akhtar, I. Robert-Philip, A. Dréau, O. Brinza, J. Achard, A. Tallaire, V. Jacques, *Diamond Relat. Mater.* **2019**, *96*, 85.
[22] J. F. Barry, J. M. Schloss, E. Bauch, M. J. Turner, C. A. Hart, L. M. Pham, R. L. Walsworth, *Rev. Mod. Phys.* **2020**, *92*, 608.
[23] M. K. Atumi, J. P. Goss, P. R. Briddon, M. J. Rayson, *Phys. Rev. B* **2013**, *88*, 24.
[24] T. Miyazaki, Y. Miyamoto, T. Makino, H. Kato, S. Yamasaki, T. Fukui, Y. Doi, N. Tokuda, M. Hatano, N. Mizuochi, *Appl. Phys. Lett.* **2014**, *105*, 261601.
[25] A. M. Edmonds, U. F. S. D'Haenens-Johansson, R. J. Cruddace, M. E. Newton, K.-M. C. Fu, C. Santori, R. G. Beausoleil, D. J. Twitchen, M. L. Markham, *Phys. Rev. B* **2012**, *86*, 3.
[26] T. R. Eichhorn, C. A. McLellan, A. C. B. Jayich, *Phys. Rev. Mater.* **2019**, *3*, 11.
[27] T. Gullion, D. B. Baker, M. S. Conradi, *J. Mag. Reson.* **1990**, *89*, 479.
[28] G. de Lange, Z. H. Wang, D. Ristè, V. V. Dobrovitski, R. Hanson, *Science* **2010**, *330*, 60.
[29] L. M. Pham, N. Bar-Gill, C. Belthangady, D. Le Sage, P. Cappellaro, M. D. Lukin, A. Yacoby, R. L. Walsworth, *Phys. Rev. B* **2012**, *86*, 479.
[30] V. M. Acosta, E. Bauch, M. P. Ledbetter, C. Santori, K.-M. C. Fu, P. E. Barclay, R. G. Beausoleil, H. Linget, J. F. Roch, F. Treussart, S. Chemerisov, W. Gawlik, D. Budker, *Phys. Rev. B* **2009**, *80*, 11.
[31] A. M. Wojciechowski, M. Karadas, C. Osterkamp, S. Jankuhn, J. Meijer, F. Jelezko, A. Huck, U. L. Andersen, *Appl. Phys. Lett.* **2018**, *113*, 013502.
[32] J. F. Barry, M. J. Turner, J. M. Schloss, D. R. Glenn, Y. Song, M. D. Lukin, H. Park, R. L. Walsworth, *Proc. Natl. Acad. Sci. USA* **2016**, *113*, 14133.

